*ceramics*

MDPI

*Article*

# 2D/2D Heterojunctions of Layered $TiO_2$ and $(NH_4)_2V_3O_8$ for Sunlight-Driven Methylene Blue Degradation

**Juan Aliaga [1], Matías Alegria [1], J. Pedro Donoso [2], Claudio J. Magon [2], Igor D. A. Silva [2], Harold Lozano [2], Elies Molins [3], Eglantina Benavente [1,*] and Guillermo González [4,*]**

[1] Departamento de Química, Facultad de Ciencias Naturales, Matemática y Medio Ambiente, Universidad Tecnológica Metropolitana, Santiago 7750000, Chile; jaliaga@utem.cl (J.A.); matias.alegriag@utem.cl (M.A.)
[2] Instituto de Física de São Carlos, Universidad de São Paulo, São Carlos 13566-590, SP, Brazil; donoso@ifsc.usp.br (J.P.D.); magon@ifsc.usp.br (C.J.M.); igor.danciaes-almeida-silva@cec.mpg.de (I.D.A.S.); harold.lozano@gmail.com (H.L.)
[3] Instituto de Ciencia de Materiales de Barcelona (CSIC), Campus UAB, 08193 Bellaterra, Spain; elies.molins@icmab.es
[4] Departamento de Química, Facultad de Ciencias, Universidad de Chile, Santiago 7750000, Chile
* Correspondence: ebenaven@utem.cl (E.B.); ggonzale@uchile.cl (G.G.)

**Abstract:** Photocatalysis based on titanium dioxide ($TiO_2$) has become a promising method to remediate industrial and municipal effluents in an environmentally friendly manner. However, the efficiency of $TiO_2$ is hampered by problems such as rapid electron–hole recombination and limited solar spectrum absorption. Furthermore, the sensitization of $TiO_2$ through heterojunctions with other materials has gained attention. Vanadium, specifically in the form of ammonium vanadate ($(NH_4)_2V_3O_8$), has shown promise as a photocatalyst due to its ability to effectively absorb visible light. However, its use in photocatalysis remains limited. Herein, we present a novel synthesis method to produce lamellar $(NH_4)_2V_3O_8$ as a sensitizer in a supramolecular hybrid photocatalyst of $TiO_2$–stearic acid (SA), contributing to a deeper understanding of its structural and magnetic characteristics, expanding the range of visible light absorption, and improving the efficiency of photogenerated electron–hole separation. Materials, such as $TiO_2$–SA and $(NH_4)_2V_3O_8$, were synthesized and characterized. EPR studies of $(NH_4)_2V_3O_8$ demonstrated their orientation-dependent magnetic properties and, from measurements of the angular variation of g-values, suggest that the $VO_2^+$ complexes are in axially distorted octahedral sites. The photocatalytic results indicate that the 2D/2D heterojunction layered $TiO_2$/vanadate at a ratio (1:0.050) removed 100% of the methylene blue, used as a model contaminant in this study. The study of the degradation mechanism of methylene blue emphasizes the role of reactive species such as hydroxyl radicals ($^\bullet OH$) and superoxide ions ($O_2^{\bullet-}$). These species are crucial for breaking down contaminant molecules, leading to their degradation. The band alignment between ammonium vanadate ($(NH_4)_2V_3O_8$) and $TiO_2$–SA, shows effective separation and charge transfer processes at their interface. Furthermore, the study confirms the chemical stability and recyclability of the $TiO_2$–SA/$(NH_4)_2V_3O_8$ photocatalyst, demonstrated that it could be used for multiple photocatalytic cycles without a significant loss of activity. This stability, combined with its ability to degrade organic pollutants under solar irradiation, means that the $TiO_2$–SA/$(NH_4)_2V_3O_8$ photocatalyst is a promising candidate for practical environmental remediation applications.

**Keywords:** titanium dioxide; heterojunction; methylene blue; photocatalytic degradation

**Citation:** Aliaga, J.; Alegria, M.; Donoso, J.P.; Magon, C.J.; Silva, I.D.A.; Lozano, H.; Molins, E.; Benavente, E.; González, G. 2D/2D Heterojunctions of Layered $TiO_2$ and $(NH_4)_2V_3O_8$ for Sunlight-Driven Methylene Blue Degradation. *Ceramics* **2024**, *7*, 926–943. https://doi.org/10.3390/ceramics7030060

Academic Editor: Gilbert Fantozzi

Received: 5 June 2024
Revised: 24 June 2024
Accepted: 25 June 2024
Published: 2 July 2024

## 1. Introduction

Photocatalysis based on titanium dioxide has garnered significant attention due to its promising ability to facilitate the remediation and reuse of industrial and municipal effluents in an environmentally benign manner [1–3]. Nonetheless, its efficiency is hampered by a high rate of hole-electron recombination and scarce absorption of the solar spectrum [4,5]. To enhance $TiO_2$ performance, researchers have explored modifications to its electronic structure and morphology. These efforts involve introducing dopants, both metallic and non-metallic elements, and creating mixed phases within the same semiconductor (e.g., $TiO_2$-P25 and black titania) to introduce new intra-bandgap levels [6–8]. Recent observations indicate that molecularly thin $TiO_2$ sheets coated on both sides with monolayers of fatty acids outperform pristine $TiO_2$ [9,10]. This improvement can be attributed to various factors, such as the creation of surfaces with abundant defects, the conjugation of nano–micro dimensions in 2D structures, and the increased hydrophobicity of particle surfaces, which is similar to that of organic contaminants. Improving the photocatalytic performance of both modified anatase and lamellar derivatives is usually limited. A more effective alternative often entails sensitizing $TiO_2$ through heterojunctions with species that not only establish electric fields to reduce electron–hole recombination rates but also as antennas, capturing lower-energy light and transferring it to $TiO_2$ [11,12].

Vanadium, a member of the first transition series ([Ar] $4s^2$ $3d^3$), forms stable aqueous species in various oxidation states (ranging from $2^+$ to $5^+$). Vanadium(V) oxide, $V_2O_5$, possesses a bandgap of 2.4–2.8 eV [13], allowing it to effectively absorb visible light [14,15]. However, its utility as a photocatalyst is limited [16]. Consequently, research has shifted its focus towards V(V)-oxosalts, especially metal metavanadates, and compounds like potassium vanadate such as $K_2V_6O_{16}$ and $KV_3O_8$ [17]. These materials have displayed photocatalytic activity, primarily due to the presence of V(IV) [17,18]. Furthermore, $V_2O_5$ has proven to be effective as a sensitizer for wide-bandgap semiconductors like $SnO_2$ [19] and $TiO_2$ [20], contributing to hydrogen evolution and tetracycline degradation, respectively. Layered hybrid nanostructures, exemplified as mixed-valence V(V)/V(IV) vanadium pentoxide ($VO_x$) nanotubes produced via hydrothermal treatment, have demonstrated their ability to sensitize ZnO for contaminant degradation under simulated sunlight [21]. Inorganic $VO_x$ nanostructures, including microsquares belonging to the $V_7O_{16}$ family [22], have received reduced attention regarding their photocatalytic properties [23,24] $(NH_4)_2V_3O_8$, which crystallizes in the fresnoite structure with a formal vanadium ion ratio of $V^{5+}/V^{4+} = 2/1$, has gained recognition for its magnetic properties [25–27] and potential use as an electrode material for lithium-ion and zinc-ion batteries [28–31]. Various studies have sought to optimize the synthesis of $(NH_4)_2V_3O_8$ to elucidate the distinctive structure–property relationship stemming from its 2D molecular architecture and paramagnetic $d^1$ electronic configuration of V(IV) [30,32,33]. Magnetic susceptibility at different temperatures and magnetic behavior has been explored using both polycrystalline [25] and oriented single-crystal samples [34]. However, to the best of our knowledge, the photocatalytic properties of $(NH_4)_2V_3O_8$ have not been reported thus far.

In this study, we present a new synthesis method to produce $(NH_4)_2V_3O_8$, X-ray diffraction (XRD) studies reveal its structure. Moreover, we investigated its orientation-dependent magnetic properties using electron paramagnetic resonance (EPR) and, evaluate its potential as a sensitizer in a $TiO_2$-based supramolecular hybrid photocatalyst.

Our research not only contributes to a deeper understanding of the structural and magnetic characteristics of $(NH_4)_2V_3O_8$, but also highlights that the $TiO_2/(NH_4)_2V_2O_8$ (1:0.05) heterojunction, which comprises around 5% of this vanadate can significantly improve the degradation rate of methylene blue. The degradation of this contaminant being approximately three times faster than with $TiO_2$–stearic acid under simulated sunlight.

## 2. Materials and Methods

### 2.1. Chemicals

All chemical reagents used in this study were of guaranteed grade and were obtained from commercial sources, $Ti[OCH(CH_3)_2]_4$ (titanium tetraisopropoxide), $C_{18}H_{36}O_2$ (stearic acid), $NH_4VO_3$ (ammonium metavanadate), $C_{16}H_{35}N$ (hexadecylamine), ($C_2H_4O_2$) glacial acetic acid, NaOH (sodium hydroxide), $C_{16}H_{18}ClN_3S$ (methylene blue), $C_8H_6O_4$ (terephthalic acid), $C_6H_4O_2$ (benzoquinone) and ($C_2H_8N_2O_4$) ammonium oxalate were purchased from Sigma-Aldrich, Saint Louis, MO, USA. ($C_2H_6O$) ethanol and $C_3H_8O$ (isopropanol) were purchased from Merck KGaA, Darmstadt, Germany. All reagents were of analytical grade and were used without further purification.

### 2.2. Sample Preparation

Diammonium trivanadate $(NH_4)_2V_3O_8$ was synthesized using a straightforward hydrothermal method. In a typical synthesis, 0.936 g of $NH_4VO_3$ and 0.966 g of hexadecylamine (HDA) were dissolved in 40 mL of ethanol with vigorous stirring. Subsequently, 4 mL of glacial acetic acid was added to the solution. After 30 min of stirring, 40 mL of deionized water (18 MΩ) was introduced, resulting in the development of a yellow color in the solution. The solution was then sealed and kept under continuous agitation in the dark. The pH of the resulting dispersion was adjusted to 6.0 using a 0.1 M NaOH solution and transferred into a Teflon-lined stainless-steel autoclave with a 15 mL capacity. The autoclave was heated to 180 °C and maintained at this temperature for 24 h. After cooling to room temperature, the resulting dark violet crystalline product was separated by centrifugation and subjected to several washes with ethanol and acetone. Finally, the sample was dried at 60 °C overnight in the open air.

Titanium Dioxide-Stearic acid Nanocomposite ($TiO_2$–SA) was synthesized following a procedure detailed in our prior work [10]. Briefly, stearic acid was blended with ethanol in an argon atmosphere and stirred for 3 h at 50 °C. Subsequently, titanium tetraisopropoxide (TTIP) was added dropwise, and the mixture was continuously stirred for an additional hour at the same temperature. This suspension was then left to age at room temperature for a week. The resulting white precipitate was separated by centrifugation, thoroughly washed with ethanol, and then dried at 45 °C for a period of 72 h.

$TiO_2$–SA/$(NH_4)_2V_3O_8$ ratios were prepared in the range of 1:0.025; 1:0.05; 1:0.10 and 1:0.15 (weight ratio). These samples were mixed manually using an agate mortar. Before exposure to irradiation, the suspension was subjected to ultrasonication for 2 min to ensure the creation of a homogeneous sample, promoting intimate contact, and reducing aggregates in sample preparation [35].

### 2.3. Characterization Methods

A single crystal of $(NH_4)_2V_3O_8$ was analyzed for intensity data collection on a Nonius Kappa CCD FR590 diffractometer with mirror-monochromatized Mo-K$\alpha$ radiation ($\lambda$ = 0.71073 Å) to confirm the cell and resolve the structure. The structures of all compounds were determined by direct methods and refined by full-matrix least-squares procedures using the SHELXTL package. The details of the crystal parameters, data collection and refinements for all the complexes are summarized in Tables S1–S4.

Samples were subjected to powder X-ray diffraction (XRD) analyses using a D8 Advance diffractometer (Bruker AXS, Karlsruhe, Germany) instrument with Cu K$\alpha$ radiation ($\lambda$ = 1.5418 Å). Continuous wave (CW) electron paramagnetic resonance (EPR) experiments were conducted at temperatures of 5.5 K and 300 K utilizing a Elexsys E580 spectrometer (Bruker Corporation, Billerica, MA, USA) operating at approximately 9.476 GHz. The spectrometer was outfitted with a continuous flow liquid helium cryogenic system (Oxford ESR900) and a temperature controller Oxford ITC503 (both Oxford Instruments, Abingdon, UK). To avoid saturation effects, the microwave power was consistently attenuated by at least 6 dB below the saturation threshold. Modulation frequency is set to 100 kHz. To prevent overmodulation and passage effects, the modulation amplitude and amplifier time constant were set to at least one tenth of the narrowest line width and shortest transit time, respectively. A single tiny crystal of $(NH_4)_2V_3O_8$ with planar dimensions measuring approximately 1 mm × 0.5 mm is stuck with silicone vacuum grease to one of the faces of a cubic block of KCl crystal of 2 mm × 2 mm × 2 mm. The width of the crystal was very small (much smaller than one mm) and, due to the material's delicate nature, it could not be measured. Subsequently, the KCl block and sample assembly were attached using the same grease to a base crafted from rexolite and secured at the bottom of a Wilmad EPR quartz sample tube (4 mm inner diameter) (Wilmad Glass, ATS Products, Warminster, PA, USA). For field calibration, an almost imperceptible grain of DPPH free radical (2,2–diphenyl–1–picrylhydrazil), with a g-factor of 2.0037, was carefully positioned adjacent to the sample, serving as an EPR marker. To facilitate rotation of the sample around the microwave cavity's symmetry axis, the sample tube was connected to a ER218PG1 goniometer (Bruker Corporation, Billerica, MA, USA). The goniometer is capable of conducting accurate and automated measurements of EPR spectra while varying both the magnetic field and goniometer angle. The initial alignment of the sample relative to the applied magnetic field is achieved visually, which may introduce a minor error of a few degrees in the estimation of initial angles. Scanning electron microscopy (SEM) images were acquired using a ZEISS Gemini SEM 360 NanoVP Carl microscope (Carl Zeiss AG, Oberkochen, Germany). The images of transmission electron microscopy (TEM) were attained using a JEOL model JEM-1400 microscope (JEOL GmbH, Freising, Germany). Diffuse reflectance UV–Vis spectra (DRS) were recorded in the range of 300–800 nm using a Jasco model V-770 spectrometer (Jasco Corporation, Tokio, Japan). Reflectance measurements were renewed to absorption spectra using the Kubelka-Munk function. Fourier transform infrared (FTIR) spectra were recorded on a Nicolet iS5 Thermo Scientific FT/IR spectrophotometer (Thermo Fisher Scientific, Waltham, MA, USA). Photoluminescence (PL) spectra were acquired using a PerkinElmer model LS 55 fluorescence spectrophotometer (Perkin Elmer, Waltham, MA, USA). UV–Vis spectra were recorded at room temperature using a Jasco, model V-730 UV–Vis spectrometer (Jasco Corporation, Tokio, Japan).

### 2.4. Photocatalytic Degradation

The photocatalytic activity of the samples was assessed under simulated solar irradiation by studying the degradation of aqueous solutions containing methylene blue (MB) as a model pollutant. The characteristic absorption peak of MB was monitored using a UV–Vis spectrophotometer. The different mixtures of $TiO_2$–SA/$(NH_4)_2V_3O_8$ with ratios ranging from 1:0.025 to 1:0.15 were combined with 25 mL of a $1 \times 10^{-5}$ mol $L^{-1}$ MB solution at a pH of 7 (buffer). Before solar irradiation measurements, the suspension was stirred magnetically in the dark for 30 min to establish an adsorption/desorption equilibrium between the dye and samples. The suspensions were exposed to a solar simulator (AM 1.5 G-1.00 kW/$m^2$ (Verasol, Newport, OR, USA). Approximately 0.5 mL of the reaction mixture was collected every 30 min, up to a total irradiation of 120 min. The samples were centrifuged to eliminate interference from suspended catalyst particles. The initial concentration of MB after adsorption/desorption equilibrium was designated as $C_0$, and the UV–Vis spectra were measured using nanopure water as a reference. To assess the reusability and chemical stability of the synthesized samples, we conducted five consecutive photocatalytic reactions. At the start of each cycle, a new load of MB was added and adjusted to a volume of 25 mL at a concentration of $1 \times 10^{-5}$ M using the same catalyst. To verify the stability of the photocatalysts, we subjected the initial sample and the samples used in the reuse experiments to XRD analysis. This was done to confirm its photostability under UV–Vis light irradiation.

To detect the presence of hydroxyl radicals during photocatalytic reactions, we utilized terephthalic acid (TA) at a concentration of 4 mmol $L^{-1}$ in an alkaline medium containing NaOH 2 M (pH 8). TA undergoes reaction with $^\bullet$OH radicals, resulting in the formation of a highly fluorescent product, 2-hydroxyterephthalic acid (TAOH). At 10 min intervals following the solar irradiation, small aliquots of the reaction solution were collected and centrifuged. These samples were then analyzed using a spectrofluorometer until the irradiation duration reached 90 min. The fluorescence product was detected with a peak emission wavelength of 426 nm and an excitation wavelength of 312 nm [36].

The reuse stability of the photocatalyst was tested with four consecutive reuses. Under similar operating conditions, reuse experiments were performed with the same catalyst. After each experiment, a new methylene blue solution, calibrated to a volume of 25 mL, was added and the same absorption intensity of the $1 \times 10^{-5}$ M concentration carried out during the experiments was determined by UV spectroscopy, at time intervals to evaluate the potential for reuse of the catalyst.

## 3. Results and Discussion

### *3.1. Synthesis and Characterization of the Precursors of the Photocatalytic System*

In general, hydrothermal treatment of hydrogels formed via the hydrolysis of $V_2O_5$ or its salt precursor leads to a partial reduction of V(V) to V(IV) vanadium ions [37,38]. The extent of this reduction depends on the treatment's conditions. In this specific case, the hydrolysis of $NH_4VO_3$ using hexadecylamine as a template resulted in the formation of a layered nanocomposite intercalated with the surfactant, resembling precursors of $V_2O_5$ hybrid structures such as nanotubes [39] and nanourchins [23]. During the alkaline hydrothermal treatment of the hydrolysis reaction product, both the partial reduction of V(V) to V(IV) and the segregation of the template occurred simultaneously, leading to the formation of 'giant' single-crystal thin plates with basal dimensions ranging from 2 to 10 mm (Figure S1). Single-crystal X-ray diffraction analysis of the as-prepared product confirmed its structural similarity to the $(NH_4)_2V_3O_8$ compound reported in the literature [40]. The crystallographic data for compounds are shown in Tables S1–S4. The $(NH_4)_2V_3O_8$ features a lamellar structure comprised of layers consisting of corner-sharing $VO_4$ tetrahedra and $VO_5$ square pyramids with the $NH_4^+$ ions lying between the layers [25,32,41]. Figure 1a showcases a high-resolution transmission electron microscopy (HRTEM) image of the as-prepared $(NH_4)_2V_3O_8$, with discernible lattice planes 100 and 010 having an interplanar distance of approximately 8.9 Å [28]. The SAED patterns confirm the single-crystal nature, and the diffraction spots can be indexed to a tetragonal $(NH_4)_2V_3O_8$ structure (Figure 1b). The $TiO_2$–SA nanocomposite was synthesized by reacting titanium tetraisopropoxide (TTIP) with stearic acid in ethanol and the mixture was allowed to age for 72 h. Infrared spectroscopy was performed to confirm the presence of stearic acid in the nanocomposite. Figure S2 shows the characteristic signals attributed to the asymmetric and symmetric stretching vibrations of the $CH_2$ groups at 2920 and 2849 $cm^{-1}$, respectively, which correspond to stearic acid. Additionally, prominent signals are observed at 1538 and 1395 $cm^{-1}$, corresponding to the asymmetric and symmetric vibration of the C=O of the carboxylic acid, indicating its interaction with titanium atoms (COO–Ti) [42]. In the lower frequency range of the spectrum, a signal at 999 $cm^{-1}$ is observed, which can be attributed to the Ti–O–C bond. Figure S3 reveals the characteristic Raman scattering of linear saturated acids, appearing at around 1100 $cm^{-1}$, 1300 $cm^{-1}$, and in the range of 1500–1400 $cm^{-1}$. These signals are assigned to various vibrational modes, including ν(CC), $CH_2$ torsion, and $CH_2$ scissor vibrations and bending $CH_3$, respectively [43]. Notably, certain features are consistent with reported vibration modes reported for ultrathin $TiO_2$(B) nanosheets [44]. The $TiO_2$–stearic acid nanocomposite exhibits a layered nanostructure, with stearic acid sandwiched between inorganic sheets, as supported by previous studies [9,10,45].

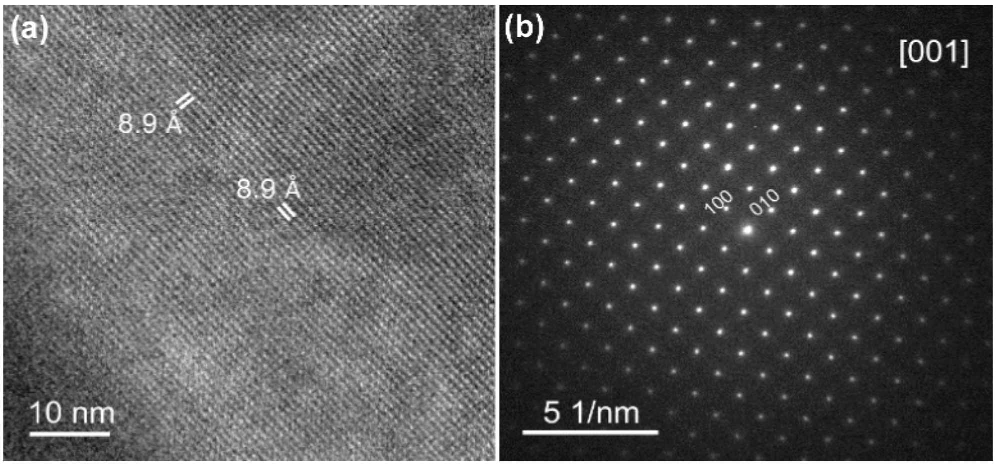

**Figure 1.** (**a**) HRTEM image; and (**b**) the SAED pattern of the as-prepared $(NH_4)_2V_3O_8$ along the [001] zone axis.

### 3.2. Electron Paramagnetic Resonance Studies of the Electronic Structure of Vanadium in the Crystal Structure of $(NH_4)_2V_3O_8$

In the crystal structure of $(NH_4)_2V_3O_8$, it is stablished that the V=O bonds align parallel to [001] direction, while the cleavage planes are perpendicular to [001]. Consequently, the V=O bonds, pivotal in determining the EPR spectrum, are perpendicular to the principal cleavage plane. Given that the behavior of the unpaired electron in a $VO^{2+}$ complex is predominantly dominated by the V=O bond, both its direction and the symmetry within the sample can be discerned through the analysis of the angular dependence of the EPR spectra.

Figure 2a illustrate the experimental setup employed to capture the angular dependence of the EPR spectrum for an arbitrary magnetic field orientation given by angles $\theta$ and $\varphi$. Remarkably, regardless of the field orientation, only one symmetric line is observed, which can be accurately fitted by a first derivative of a Lorentzian lineshape. Notably, when the magnetic field lies on the $xy$ plane ($\theta = 90°$) the EPR spectra exhibit no angular dependence on $\varphi$ (results are not displayed); therefore, the angular variations presented herein are solely in relation to the angle $\theta$. When the magnetic field is rotated within the $xz$ plane, a pronounced dependence on $\theta$ is evident, as illustrated in Figure 2b. This figure presents three selected spectra at $\theta$ angles of 0°, 45° and 90° for both measuring temperatures of 300 K and 5.5 K. At 300 K, the data exhibit a discernable increase in line intensity from $\theta = 0°$ to $\theta = 90°$, attributed to an increase of the linewidth, as will be elucidated subsequently. Conversely, the behavior of the line intensity at 5.5 K demonstrates a distinct pattern. Specifically, at 5.5 K, the line intensity decreases from $\theta = 0°$ to $\theta = 45°$, followed by an increase towards $\theta = 90°$. This distinctive behavior will be discussed later. The lack of resolved hyperfine interactions with $^{51}V$ nuclei ($I = 7/2$, 99.8% natural abundance) on the EPR line suggests that the unpaired electron spins are influenced by exchange interactions. These interactions lead to a significant exchange narrowing effect, which effectively smears out the hyperfine structure.

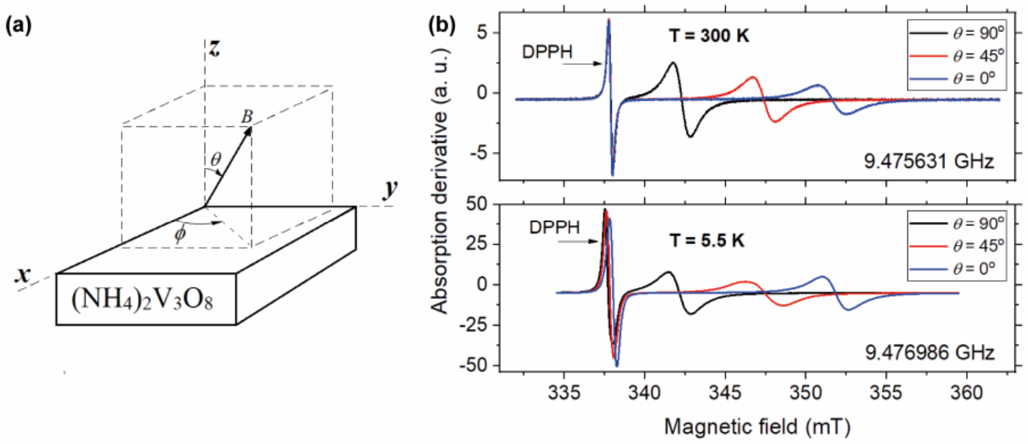

**Figure 2.** (**a**) A schematic representation of the experimental arrangement. The $(NH_4)_2V_3O_8$ symmetry plane is aligned with the $xy$ plane. The $z$-axis is chosen to be perpendicular to the $xy$ crystal plane. Angles $\theta$ and $\varphi$ define the orientation of the applied magnetic field $B$; and (**b**) CW-EPR spectra of $(NH_4)_2V_3O_8$ (and marker DPPH) for selected angles, 0° (blue line), 45° (red line), 90° (black line), measured at temperatures of 300 K and 5.5 K, for an arbitrary angle $\varphi$. Microwave frequencies are indicated. The EPR lines below 340 mT are from the DPPH standard $g$-marker, while the remaining are from the studied sample.

The angular variation of the EPR spectra was conducted by measuring the spectra at interval $\Delta\theta = 5°$, ranging from $\theta = -87°$ to $\theta = +113°$. Given that $\theta = 0°$, the magnetic field is parallel to the V=O bond; this orientation is designated as the parallel direction. Consequently, $\theta = 90°$ corresponds to the perpendicular direction. Figure 3 depicts the results obtained for the angular variation of the EPR spectra of $(NH_4)_2V_3O_8$ at temperatures of 300 K and 5.5 K. The DPPH spectra are isotropic and are not shown in the figure.

However, as observed in Figure 2b, the central field of the DPPH line undergoes slight shifts relative to the angle, particularly noticeable at 5.5 K, owing to small microwave frequency variations.

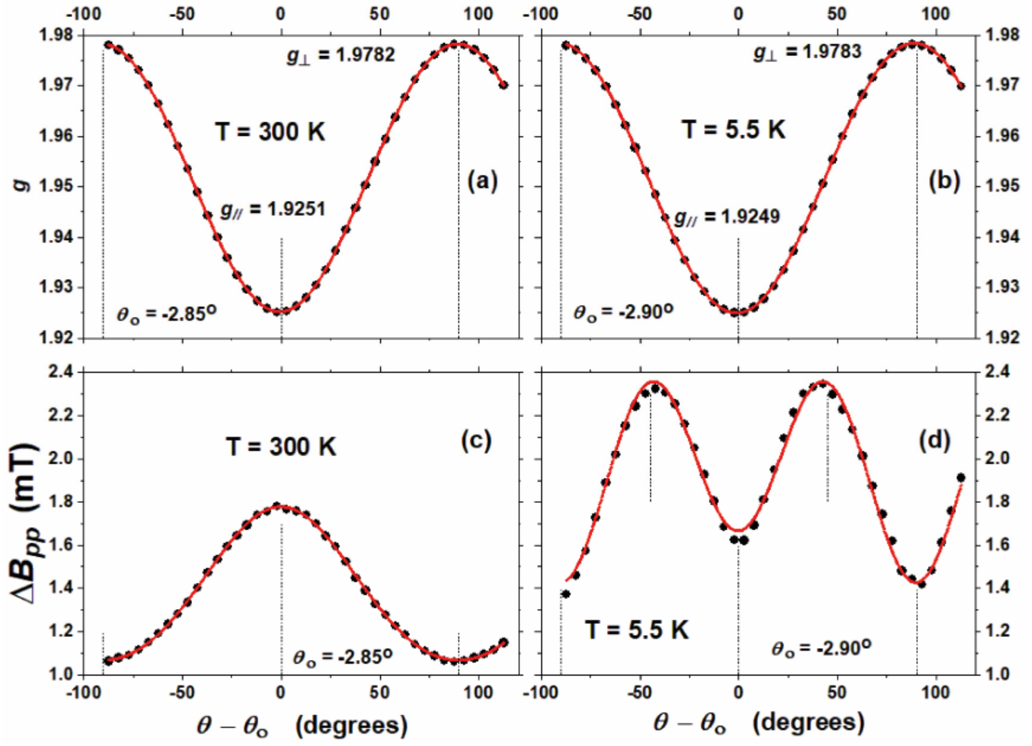

**Figure 3.** (**a**,**b**) Angular variation of the *g*-value; and (**c**,**d**) linewidth measured at 300 K and 5.5 K, respectively, for the applied magnetic field along the *xz* plane. Black circles are the experimental data and solid red lines represent the numerical simulation of the respective parameters. Vertical dashed lines denote the values of $\theta - \theta_o$ at 0°, ±45° and ±90°. Microwave frequencies: 9.475631 GHz (300 k) and 9.476986 GHz (5.5 K).

The least-square fitting of the spectra, based on the first derivative of a Lorentzian lineshape, enables the extraction of the line parameters such as the central position, peak-to-peak amplitude, and peak-to-peak width. Despite the slight asymmetry in the DPPH lineshape, a Lorentzian fitting proves sufficiently accurate for determining its central field. The g-values of the unpaired electron in the $VO^{2+}$ complex are computed from the resonance condition.

$$h\nu = \beta g B_o \ \text{ and } \ g = g_m \frac{B_m}{B_o} \tag{1}$$

On the left side, $\beta$ represents the Bohr magneton, $\nu$ denotes the microwave frequency and $h$ stands for Plank's constant. On the right side, $B_m$ and $g_m$ = 2.0037 are the central field and *g*-value of the DPPH marker, respectively. $B_o$ and $g$ represent the central field position and *g*-value of the sample spectrum, respectively. The microwave frequency is precisely locked onto the resonant frequency of the cavity. However, due to the rotation of the sample and fluctuations in room temperature, a minor change in the microwave frequency was anticipated throughout the experiment. Therefore, to account for this variability, the formula on the right was consistently employed.

Analysis of the results presented in Figure 3a,b reveals a cosine-like angular variation of the g-values as a function of $\theta$. This variation in the g-values concerning the rotation angle can be analyzed through the expression derived from the Zeeman interaction:

$$g = \sqrt{g_\perp^2 sin^2\left(\theta - \theta_0\right) + g_\parallel^2 cos^2\left(\theta - \theta_0\right)} \tag{2}$$

where $g_{\parallel}$ and $g_{\perp}$ represent the parallel and the perpendicular components of the $g$-tensor, respectively, and $\theta_0$ denotes an angular correction resulting from imprecision in setting the initial sample position (values are indicated in the figure). The fitting of the experimental data with this function is shown in solid red lines in Figure 3a,b, with the fitting parameters detailed in Table 1.

**Table 1.** EPR parameters obtained from the experimental data.

| Temperature | $g_{\perp}$ | $g_{\parallel}$ | A (mT) | B (mT) | C (mT) |
|---|---|---|---|---|---|
| 300 K | 1.9782 | 1.9251 | 1.751 | −0.779 | 0.0236 |
| 5.5 K | 1.9783 | 1.9249 | 2.022 | 0.838 | −0.359 |

The principal values of the $g$-tensor are $g_{\parallel}$ =1.925 ± 0.001 and $g_{\perp}$ = 1.978 ± 0.001. These values align closely with those previously reported for $(NH_4)_2V_3O_8$, $g_{\parallel}$ = 1.9263 and $g_{\perp}$ = 1.9755 [34] and are also consistent with those documented for $K_2V_3O_8$, a vanadium oxide belonging to the same crystallographic group as $(NH_4)_2V_3O_8$: $g_{\parallel}$ = 1.922 and $g_{\perp}$ = 1.972 [26]. The fact that $g_{\parallel} < g_{\perp} < g_e$, where $g_e$ = 2.0023 represents the free electron $g$-value, suggests that the $VO^{2+}$ paramagnetic centers are located in axially distorted octahedral sites. The unpaired electron is located in the $3d_{xy}$ orbital of the transition metal ion. The relationships of $g_{\parallel}$, $g_{\perp}$ and $g_e$ are observed across various vanadyl complexes and also in glasses doped with vanadium, as documented in the literature [46–49]. The tetragonality of the $VO^{2+}$ sites are determined by the parameter $(\Delta g_{\parallel}/\Delta g_{\perp})$ where $\Delta g_{\parallel} = (g_e - g_{\parallel})$ and $\Delta g_{\perp} = (g_e - g_{\perp})$. The ratio $(\Delta g_{\parallel}/\Delta g_{\perp})$ = 3.2 of $(NH_4)_2V_3O_8$ suggests that the vanadyl ions experience slight tetragonal distortion within the octahedral sites. It is interesting to note that this ratio aligns consistently with those reported for $VO^{2+}$ and $V^{4+}$ in several crystalline and amorphous matrices [46,49].

The linewidth of the sample spectrum is determined by measuring the field distance between the maximum and minimum points of the first-derivative spectrum, denoted by $\Delta B_{pp}$. The peak-to-peak linewidth data are shown in Figure 3c,d, revealing noticeable distinctions at both temperatures. At 300 K, the curve assumes a bell-shaped form, whereas at 5.5 K, an M-shaped curve is observed for the angular dependence of the linewidth. A plausible mechanism accounting for the observed phenomena relates to the magnetic nature of the compound. Static susceptibility measurements at a high magnetic field demonstrate a paramagnetic behavior, accompanied by antiferromagnetic interactions among $V^{4+}$ ions in adjacent planes oriented parallel to (001), resulting in a transition temperature of around 0.5 K. This fact is consistent with our findings of Lorentzian EPR lineshapes observed across all temperatures and angles.

The lineshapes offer some evidence of critical behavior at temperatures near the transition [50]. Within the critical region, it is anticipated that, owning to critical slowing-down, the modulation induced by exchange interactions become less efficient in averaging dipolar terms. This phenomenon should result in broader linewidth and a more Gaussian-like character for the EPR lineshapes [50]. From our analysis, we infer that the measurements presented here were conducted well above the critical region.

Given the magnetic properties of the material, it has been noted that the angular dependence of the EPR linewidth can be described by the following expression [50]:

$$\Delta B_{pp} = A + Bsin^2\left(\theta - \theta_0\right) + C\left[3sin^2\left(\theta - \theta_0\right) - 1\right]^2 \quad (3)$$

where $A$, $B$ and $C$ are constants.

The solid lines depicted in Figure 3 represent the results of the fitting procedure applied to the experimental data using this formula, and the corresponding parameters are presented in Table 1. The $\sin^2\theta$ term corresponds to relaxation induced by the exchange interaction, while the $(3\sin^2\theta - 1)^2$ term is attributed to relaxation driven by spin diffusion. Transitioning from room temperature to 5.5 K, the parameters $B$ and C change signs, while the absolute value of $C$ increases by more than one order of magnitude. This indicates that, with decreasing temperature, the relaxation facilitated by spin diffusion becomes increasingly significative relative to the relaxation influenced by exchange interactions.

Further evidence for the magnetic nature of the interactions between $V^{4+}$ ions is the angular dependence of the integrated area of the EPR absorption spectra. The value of the area is calculated by means of the parameters derived from the Lorentzian fitting of the measured lineshapes of both the sample and marker, employing the well-known formula $S = \left(\pi/\sqrt{3}\right) I_{pp} \Delta B_{pp}^{2}$, where $I_{pp}$ and $\Delta B_{pp}$ are the peak-to-peak amplitude and width of the first derivative signal, respectively. The results are shown in Figure 4. On the vertical scale, the term "relative intensity" means 100 $\left(S - \hat{S}\right)/\hat{S}$, where $\hat{S}$ denotes the average of $S$ across all angles. In Figure 4, it is apparent that the DPPH signal amplitude does not remains constant, as expected, most probably due to a slight misalignment of the sample from the central axis of the microwave cavity. At 300 K the variations in the relative intensity are within the order of ±5% for both the sample and marker. However, at 5.5 K, while the fluctuation of the DPPH relative intensity remains at a similar amplitude, the variation in the sample signal noticeably increases in magnitude, revealing a pattern reminiscent of the previously observed M-shaped angular dependence in the linewidth.

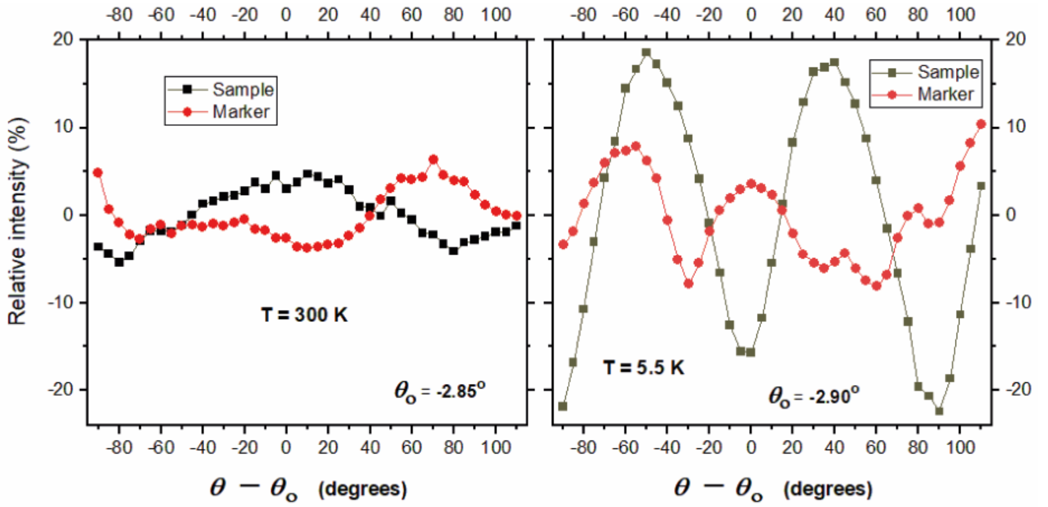

**Figure 4.** Angular variation of the relative intensity of the EPR lineshapes measured at 300 K and 5.5 K, for the applied magnetic field along the *xz* plane.

The angular dependence behavior observed for the EPR absorption integrated area of the studied sample may have an explanation based on the dynamic of the magnetic interactions. It is well-known that a Lorentzian lineshape lacks physical meaning, as evidenced by the divergence of all its even moments. Therefore, a potential error in the calculation of the area or relative intensity, as described, is the lack of knowledge about the tails of the EPR lineshapes, which remain undetectable due to being well below the baseline noise. Consequently, it is important to emphasize that, under typical circumstances, the area of a Lorentzian lineshape cannot be measured experimentally. Indeed, according to basic EPR theory, the Lorentzian profile at the tails must exhibit a "cutoff" point, beyond which a transition to Gaussian behavior occurs. In this context, we propose that the threshold marking the shift in the dynamics of the paramagnetic system is angular-dependent; potentially providing a qualitative explanation for the observed line intensity behavior.

### 3.3. Characterization Heterojunction $TiO_2$–SA/$(NH_4)_2V_3O_8$

Figure 5a illustrates the X-ray diffraction (XRD) pattern of the prepared samples $(NH_4)_2V_3O_8$, $TiO_2$–SA, and $TiO_2$–SA/$(NH_4)_2V_3O_8$ (1:0.05). The pattern of the $(NH_4)_2V_3O_8$ exhibits characteristic peaks that closely match the reported values, with the two diffraction peaks at 15.9 and 31.8 in $2\theta$ clearly indexed to the (001) and (002) planes (JCPDS 511733). In the diffractogram of $TiO_2$–SA, three consecutive and evenly spaced signals are observed at 3.2°, 6.2° and 9.2° in $2\theta$, which are attributed to the formation of structures with a preferred arrangement of stacked sheets [45]. Signals appearing between 20° and 22° in $2\theta$ indicate the presence of a small amount of free stearic acid (JCPDS 03-0252). Finally, in the diffractogram corresponding to the $TiO_2$–SA/$(NH_4)_2V_3O_8$ (1:0.050) sample, all the signals of both semiconductors are distinguishable. This suggests the coexistence of both structures in a single material, without any detectable changes or impurities apparent in the material.

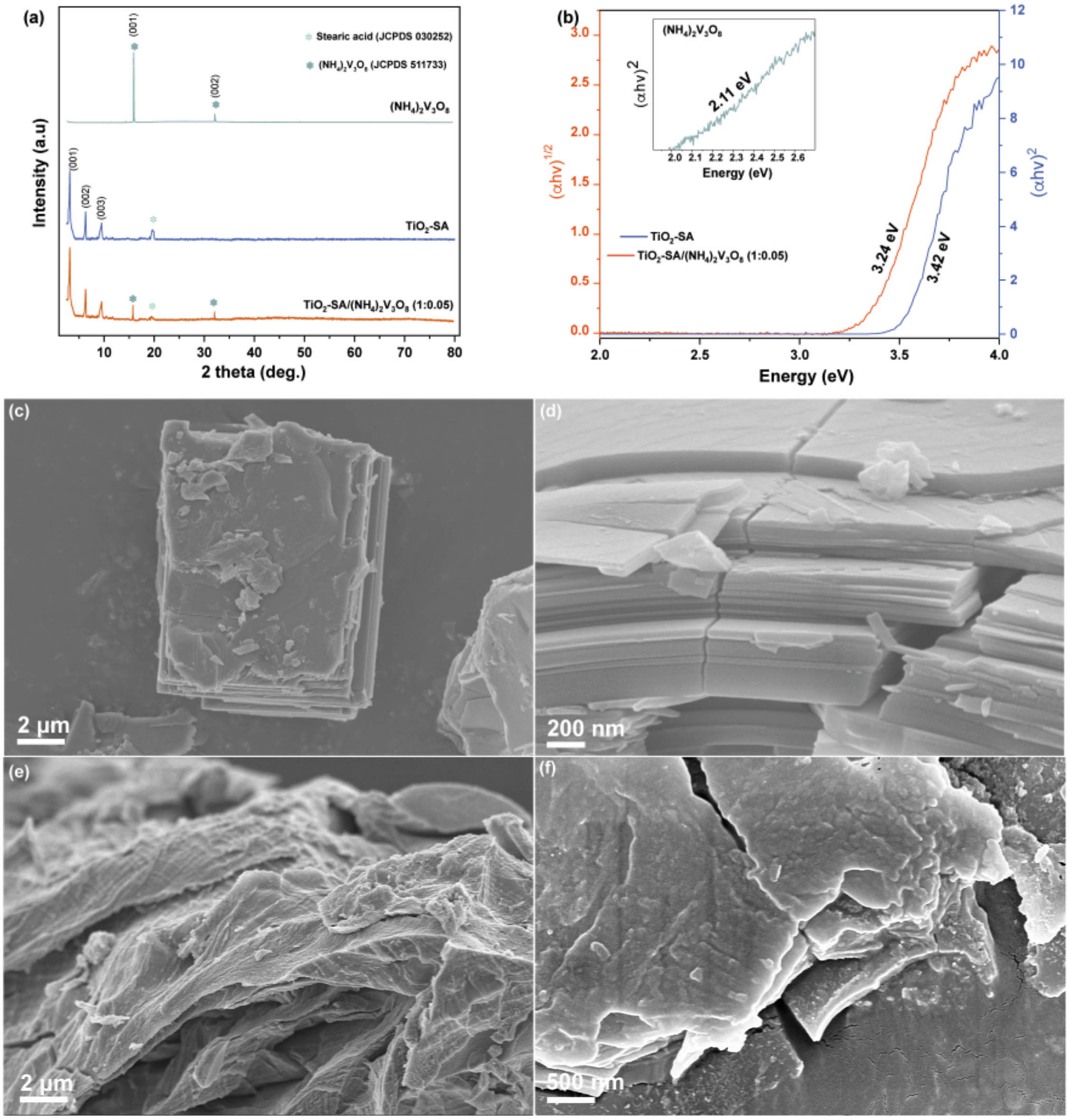

**Figure 5.** (**a**) X-ray diffraction (XRD) patterns of composites; (**b**) diffuse reflectance spectra of composites; (**c**,**d**) SEM images of $(NH_4)_2V_3O_8$; (**e**) SEM image of $TiO_2$–SA; and (**f**) SEM image of $TiO_2$–SA/$(NH_4)_2V_3O_8$.

Diffuse reflectance spectroscopy (DRS) was employed to characterize the samples. The bandgap of the samples was determined using the Tauc method, with energy (Eg) calculated from the plots of $(\alpha h\nu)^{1/2}$ and $(\alpha h\nu)^2$ for indirect and direct transitions, respectively, against photon energy. The bandgap values were obtained by analyzing the intercept of a tangent to the x-axis. As illustrated in the insert in Figure 5b [51]. $(NH_4)_2V_3O_8$, demonstrates a broad absorption within the visible light range, and indicates an indirect band gap width of 2.11 eV [41]. In contrast, $TiO_2$–SA displays a direct bandgap of 3.42 eV [45]. However, in the case of the $TiO_2$–SA/$(NH_4)_2V_3O_8$ (1:0.050) composite, an indirect bandgap of 3.24 eV is observed, signifying a noticeable shift in the sample's absorption capacity. This shift suggests a synergistic effect between the two semiconductors, potentially enhancing the composite's light absorption capability. Figure 5c,d display the scanning electron microscopy (SEM) images for $(NH_4)_2V_3O_8$. These images reveal the formation of crystals with a square and uniform morphology, characterized by sizes exceeding 5 µm formed by a two-dimensional layered structure. In Figure 5e, the $TiO_2$–SA nanostructures are evident, showing the formation of arrangements consisting of thin sheets with rounded and stacked edges, with each having lengths of approximately 100–200 nm. This morphology is attributed to the layered nanocomposite structure [10]. EDS spectrum and elemental mapping images (Figure S4) demonstrate that $TiO_2$–SA/$(NH_4)_2V_3O_8$ comprises Ti, N, O and V, as expected. Notably, the incorporation of $(NH_4)_2V_3O_8$ into $TiO_2$–SA did not alter the morphology of the final composite $TiO_2$–SA/$(NH_4)_2V_3O_8$ (1:0.050), where a clear and homogeneous mixture between both components is observed (Figure 5f).

### *3.4. Photocatalytic Properties of $TiO_2$–SA/$(NH_4)_2V_3O_8$ Composites*

The adsorption capacity and photocatalytic activity of the prepared materials were assessed for removal by first adsorbing and then degrading methylene blue, a synthetic organic dye widely employed in the textile industry. The adsorption/desorption equilibration curves were obtained under dark conditions to determine the equilibration time. Figure S5 displays the results of dye adsorption using the prepared materials. It is evident that $(NH_4)_2V_3O_8$ exhibits a low capacity for adsorbing the contaminant. In contrast, when 0.025, 0.05, 0.10 and 0.15 moles of $(NH_4)_2V_3O_8$ are incorporated into $TiO_2$–SA, a significant decrease in dye concentration is observed within the first 30 min. This decrease remains constant over time, indicating the saturation of the active sites on the materials with adsorbed molecules. The percentage of dye removal after reaching the equilibrium is as follows: 1.74% for $(NH_4)_2V_3O_8$, 10.5% for $TiO_2$–SA, 16.4% for $TiO_2$–SA/$(NH_4)_2V_3O_8$ (1:0.025), 14.5% for $TiO_2$–SA/$(NH_4)_2V_3O_8$ (1:0.050), 18.3% for $TiO_2$–SA/$(NH_4)_2V_3O_8$ (1:0.10), and 22.6 for $TiO_2$–SA/$(NH_4)_2V_3O_8$ (1:0.15). The adsorption capacity of the prepared materials can be attributed to the surface area, primarily due to the lamellar structures of samples. Additionally, the presence of the organic component in $TiO_2$–SA enhances adsorption due to its affinity for the adsorbate [45]. In Figure 6a, the efficiency of MB degradation is demonstrated in the presence of $TiO_2$–SA/$(NH_4)_2V_3O_8$ samples with varying amounts of ammonium vanadium in molar ratios of 1:0.025, 1:0.050, 1:0.10, 1:0.15, as well as $TiO_2$–SA and $(NH_4)_2V_3O_8$ individually. The degradation efficiency was quantified by the ratio $C/C_0$, where $C_0$ represents the initial concentration of MB after equilibrium adsorption–desorption, and C is the concentration during the reaction.

It is notable that $TiO_2$–SA and $(NH_4)_2V_3O_8$ exhibit relatively lower degradation efficiencies, with 54% and 8% degradation, respectively, than the $TiO_2$–SA/$(NH_4)_2V_3O_8$ nanocomposites. The photocatalytic activity of the heterojunction is influenced by the concentration of $(NH_4)_2V_3O_8$. The $TiO_2$–SA/$(NH_4)_2V_3O_8$ percentage of dye degradation is as follows: 64.1% for $TiO_2$–SA/$(NH_4)_2V_3O_8$ (1:0.025), 100% for $TiO_2$–SA/$(NH_4)_2V_3O_8$ (1:0.050), 83.1% for $TiO_2$–SA/$(NH_4)_2V_3O_8$ (1:0.10), and 68.8% for $TiO_2$–SA/$(NH_4)_2V_3O_8$ (1:0.15). The heterojunction (1:0.050) exhibits optimal efficiency in the photodegradation of MB. However, with higher concentrations of the ammonium vanadate, the photocatalytic activity decreases. This decline is likely due to excess vanadium, which increases the opacity of the sample, thus blocking light absorption and potentially affecting the absorption of visible light. The reactions follow a pseudo-first-order kinetics. The apparent rate constant ($k$) is determined by fitting on $-\mathrm{Ln}(C/C_0)$ versus reaction time, as shown in Figure 6b. The results indicate that $TiO_2$–SA/$(NH_4)_2V_3O_8$ (1:0.050) exhibits significantly enhanced photocatalytic degradation, being approximately three times faster than $TiO_2$–SA. This enhancement can be attributed to the two-dimensional morphology, characterized by the sheet-like arrangement of $(NH_4)_2V_3O_8$. This morphology promotes effective "face to face interfacial contact" [52] with the surfaces of the $TiO_2$–SA, facilitating absorption in the visible range and confirming the synergistic effect between both semiconductors in $TiO_2$–SA/$(NH_4)_2V_3O_8$.

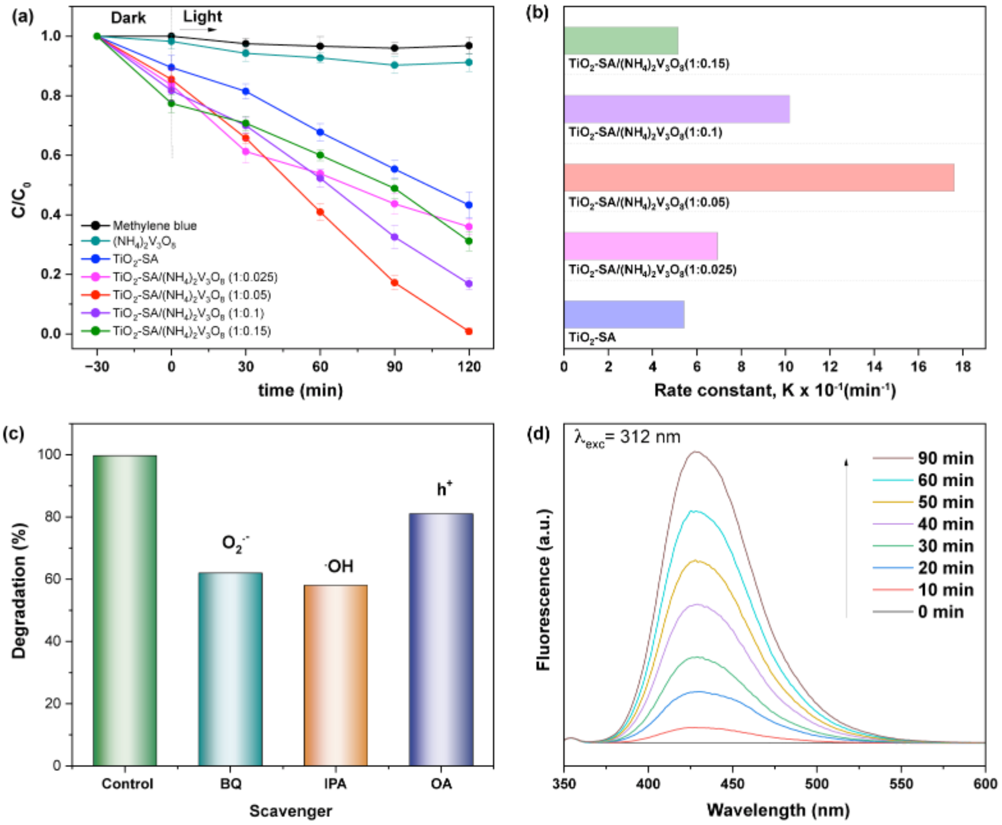

**Figure 6.** (**a**) Photocatalytic degradation of MB in the presence of the nanocomposites with molar ratios of 1:0.025, 1:0.05, 1:0.01, 1:0.15; (**b**) first-order kinetic fitting curves for MB; (**c**) photocatalytic degradation of MB in the presence of radical scavengers; and (**d**) photoluminescence (PL) spectrum of terephthalic acid (TA).

### *3.5. Degradation Mechanism*

In order to identify the species responsible for the degradation of the dye, we conducted photocatalytic tests employing the following three scavenger agents: 2-propanol (IPA), benzoquinone (BQ), and ammonium oxalate (AO). These agents selectively react with $^\bullet$OH, $O_2^{\bullet-}$ and $h^+$, respectively, thereby modulating the photocatalytic efficiency of the system under investigation. The results are presented in Figure 6c. The addition of benzoquinone (BQ) resulted in a 38% decrease in photocatalytic activity. This decrease suggests the involvement of photogenerated superoxide ($O_2^{\bullet-}$) in the photocatalytic process. Subsequently, when we repeated the experiments with the addition of 2-propanol (IPA) to the system, the concentration of the dye in the solution decreased by 42% compared to the control (no scavengers added). This finding indicates that hydroxyl radicals are also active participants in the photocatalytic process. Finally, upon incorporating ammonium oxalate, dye degradation of the dye decreased by 19%. This suggests that the primary species responsible for dye photodegradation are those generated in the transition of the electron from the valence band to the conduction band. Furthermore, the reactivity of $^\bullet$OH radicals in the degradation process was examined using photoluminescence (PL) with terephthalic acid (TA). The rates of $^\bullet$OH generation in an aqueous solution were determined under irradiation. Since TA can react with $^\bullet$OH radicals to produce fluorescent 2-hydroxyterephthalic acid (TAOH), the intensity of the PL peak indicates the quantity of $^\bullet$OH radicals produced. Figure 6d demonstrates the production of $^\bullet$OH radicals, indicating an enhancement in photocatalytic activity.

The electronic band alignment in $TiO_2$–SA/$(NH_4)_2V_3O_8$ is significant for understanding the charge transfer processes within the heterojunctions and the potential mechanisms behind the photocatalytic degradation of MB. The effectiveness of the photocatalyst depends on the effective separation of electron–hole pairs, and the migration of the photogenerated charge is closely linked to the band position in the conduction band (CB) and valence band (VB) of the semiconductors. The positions of the bands (CB and VB) for $TiO_2$–SA were calculated using the following equations from the literature [53]:

$$EVB = \chi - Ee - Eg \tag{4}$$

$$ECB = EVB - Eg \tag{5}$$

Here, $\chi$ represents the absolute electronegativity of semiconductors, with values of approximately 5.81 for $TiO_2$ and 6.10 for $(NH_4)_2V_3O_8$ [53], respectively. Ee stands for the energy of free electrons on the hydrogen scale, which is approximately 4.5 eV. The bandgap energy (Eg) of the semiconductor is determined from data obtained through diffuse reflectance spectroscopy (DRS). The calculated CB and VB edge positions of the hybrid $TiO_2$ were determined to be −0.42 eV and 3.02 eV. In the case of ammonium vanadate, the CB and VB edge positions were determined to be 0.5 eV and 2.6 eV, based on the reference [54]. When semiconductors with varying energy levels come into contact, it typically leads to a redistribution of electric charges, resulting in a shift in the positions of the band edge. This phenomenon is known as the Fermi level alignment. This results in the equal distribution of electrons and holes locating on the $TiO_2$–SA and $(NH_4)_2V_3O_8$ species at the interface of $TiO_2$–SA and $(NH_4)_2V_3O_8$ [55]. Consequently, the CB and VB of $(NH_4)_2V_3O_8$ move upward [54,56,57]. The energy band diagram of the $TiO_2$–SA and $(NH_4)_2V_3O_8$ heterostructure photocatalyst next to the thermodynamic equilibrium is depicted in Figure 7. The CB potential (CB) of an n-type semiconductor has a more negative potential (approximately 0.1–0.2 V) than the flat-band potentials [58], resulting in a Fermi level of −0.32 eV in $TiO_2$. On the other hand, $(NH_4)_2V_3O_8$ is considered an intrinsic semiconductor, and its Fermi level is situated in the middle of the conduction and valence band, at approximately 1.06 eV [59]. This causes the CB and VB levels to shift from 0.5 eV to −0.96 eV and from 2.6 eV to 1.15 eV, respectively. Therefore, we proposed a mechanism under illumination in which the photogenerated electrons are excited from the VB to the CB in both $(NH_4)_2V_3O_8$ and $TiO_2$–SA, leaving holes in VB of $(NH_4)_2V_3O_8$ and $TiO_2$–SA. Consequently, the CB of $(NH_4)_2V_3O_8$ shifts upward (towards less negative energy), while the VB of $TiO_2$–SA shifts downward (more positive energy). This generates an electric field that leads to charge transfer and the recombination of electrons in the CB of $TiO_2$–SA with the holes located in the VB of $(NH_4)_2V_3O_8$ [20]. As a result, high redox carriers are produced with holes in the $TiO_2$–SA responsible for the oxidation. The photoinduced holes in VB of $TiO_2$–SA can oxidize adsorbed $H_2O$ molecules to produce $^{\bullet}OH$ ($^{\bullet}OH/H_2O$ is 2.34 eV vs. NHE). Photogenerated electrons in the CB of $(NH_4)_2V_3O_8$ produce $O_2^{-\bullet}$ from dissolved $O_2$ since the CB position is more positive than the potential of $O_2/O_2^{-\bullet}$ (−0.33 V vs. NHE), and the reduction potential of $O_2/H_2O_2$ is 0.695 eV vs. NHE. This implies that electrons can react with $O_2$ and $H^+$ to produce $H_2O_2$, which indirectly generates $^{\bullet}OH$ [60]. These radicals can efficiently degrade methylene blue.

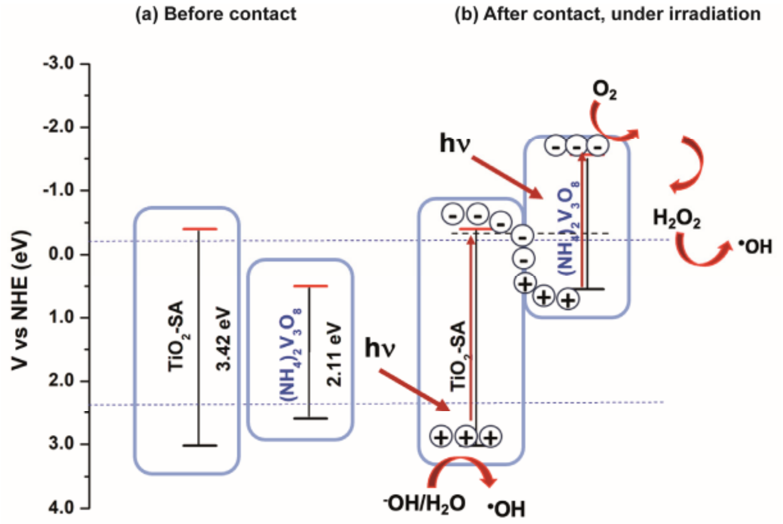

**Figure 7.** Schematic proposed photocatalytic reaction mechanism of the $TiO_2$–SA/$(NH_4)_2V_3O_8$ heterojunction.

Furthermore, the XRD analyses demonstrated the stability of the sample after undergoing consecutive photocatalytic reactions, confirming its recyclability and the ability to reuse without a significant loss of degradation efficiency (Figure 8a). Figure 8b shows the X-ray diffraction (XRD) analysis supporting the structural stability of the heterostructure catalyst.

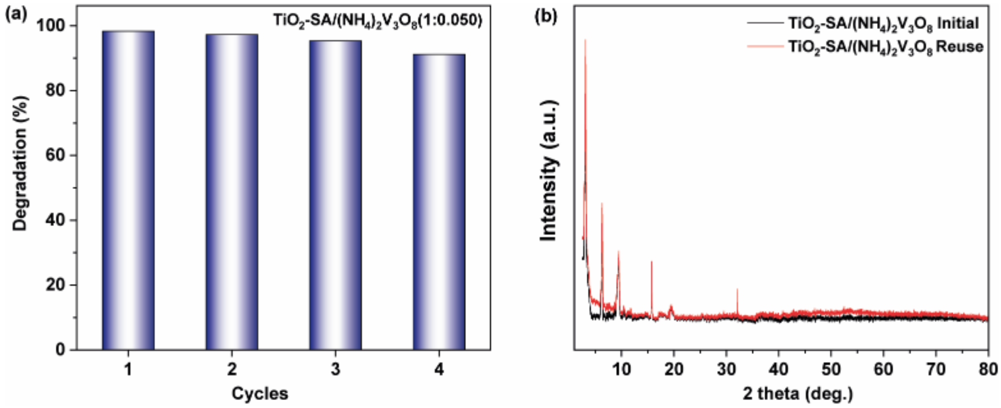

**Figure 8.** (**a**) Cycling degradation efficiency of $TiO_2$–SA/$(NH_4)_2V_3O_8$ heterojunction; and (**b**) diffraction (XRD) pattern of $TiO_2$–SA/$(NH_4)_2V_3O_8$.

## 4. Conclusions

In conclusion, this manuscript presents a novel approach for synthesizing $(NH_4)_2V_3O_8$ and demonstrates its potential application as a sensitizer in a $TiO_2$-based supramolecular hybrid photocatalyst. The research fills a significant gap in the literature by providing a thorough investigation into the structural, magnetic, and photocatalytic properties of $(NH_4)_2V_3O_8$, which have not been reported previously. The synthesis method resulted in the production of $(NH_4)_2V_3O_8$, as confirmed by X-ray diffraction. The lamellar structure of $(NH_4)_2V_3O_8$ was observed through transmission electron microscopy (TEM), with high-resolution TEM images revealing the lattice fringes of the material.

From measurements of the angular variation of $g$-values, the EPR technique applied to a sample of $(NH_4)_2V_3O_8$ suggests that the $VO^{2+}$ complexes are located in axially distorted octahedral sites. EPR lineshapes are Lorentzian for all orientations of the crystal, indicating that the measurements were taken in the paramagnetic state under the regime of exchange narrowing. Lineshape parameters, such as linewidth, peak amplitude and integrated area are compatible with the paramagnetic behavior with an antiferromagnetic interaction between $V^{4+}$ ions in consecutive layers.

Combining $(NH_4)_2V_3O_8$ with a $TiO_2$–stearic acid nanocomposite ($TiO_2$–SA) resulted in a significant improvement in photocatalytic activity for the degradation of methylene blue. This enhancement can be attributed to the 2D morphology of $(NH_4)_2V_3O_8$ sheets, which promotes efficient light absorption in the visible range, thereby demonstrating a synergistic effect between the two semiconductors in $TiO_2$–SA/$(NH_4)_2V_3O_8$.

The degradation mechanism of methylene blue involves the generation of various reactive species, including hydroxyl radicals ($^{\bullet}OH$) and superoxide ions ($O_2^{\bullet-}$), which contribute to the degradation process. The band alignment between $(NH_4)_2V_3O_8$ and $TiO_2$–SA was discussed, highlighting the efficient charge separation and transfer processes occurring at their interface. Importantly, the study also confirmed the stability and recyclability of the $TiO_2$–SA/$(NH_4)_2V_3O_8$ photocatalyst through multiple photocatalytic cycles, making it a promising candidate for practical applications in the remediation of organic contaminants under solar irradiation.

In summary, the research presented in this manuscript not only advances our understanding of the structural and photocatalytic properties of $(NH_4)_2V_3O_8$ but also highlights its potential for use in environmentally benign photocatalytic processes, contributing to the field of advanced materials for water treatment and pollutant degradation.

**Supplementary Materials:** The following supporting information can be downloaded at: https://www.mdpi.com/article/10.3390/ceramics7030060/s1, Figure S1: Singles crystal thin plates and crystal lattice structure for the unit cell; Figure S2: Infrared spectra of $TiO_2$-stearic acid; Figure S3: Raman spectra of $TiO_2$-stearic acid; Figure S4: EDS spectra and elemental mapping images $TiO_2$–SA/$(NH_4)_2V_3O_8$ (1:0.050); Figure S5: Adsorption/desorption equilibration of composites; Table S1: Crystal data and structure refinement for $(NH_4)_2V_3O_8$; Table S2: Atomic coordinates ($\times 10^4$) and equivalent isotropic displacement parameters ($Å^2 \times 10^3$) for $(NH_4)_2V_3O_8$. U(eq) is defined as one third of the trace of the orthogonalized Uij tensor; Table S3: Bond lengths [Å] and angles [°] for $(NH_4)_2V_3O_8$; Table S4: Anisotropic displacement parameters ($Å^2 \times 10^3$) for $(NH_4)_2V_3O_8$. The anisotropic displacement factor exponent takes the form: $-2p^2[h^2a^{*2}U^{11} + \ldots + 2\,h\,k\,a^*\,b^*\,U^{12}]$.

**Author Contributions:** Conceptualization J.A., M.A. and H.L.; methodology J.A. and M.A.; validation, J.A., M.A. and H.L.; formal analysis J.P.D., C.J.M., I.D.A.S., E.M. and H.L.; investigation J.P.D., C.J.M., E.M., E.B. and G.G.; writing—original draft preparation H.L., J.P.D., C.J.M. and E.B.; writing—review and editing J.A., J.P.D., C.J.M., E.B. and G.G.; visualization E.B. and G.G.; Supervision G.G. All authors have read and agreed to the published version of the manuscript.

**Funding:** Financial supported by Projects by Universidad de Chile ENL12/23, FONDECYT/ANID grant 11200609, FONDEQUIP RAMAN EQM 140142. Project supported by the Competition for Research Regular Projects, year 2023, code LCLI23-03, Universidad Tecnológica Metropolitana. Financial support by the Brazilian agencies Capes and CNPq is gratefully acknowledged. This research was partially financed by the CeRTEV, Center for Research, Technology and Education in Vitreous Materials, FAPESP 2013/07793-6.

**Institutional Review Board Statement:** Not applicable.

**Informed Consent Statement:** Not applicable.

**Data Availability Statement:** Data are available from the authors upon request.

**Acknowledgments:** We want to thank a student, Pablo Cortes, for help with experimental measurements.

**Conflicts of Interest:** The authors declare no conflicts of interest.

## References

1. Velempini, T.; Prabakaran, E.; Pillay, K. Recent Developments in the Use of Metal Oxides for Photocatalytic Degradation of Pharmaceutical Pollutants in Water—A Review. *Mater. Today Chem.* **2021**, *19*, 100380. [CrossRef]
2. Lebeau, B.; Jonas, F.; Gaudin, P.; Bonne, M.; Blin, J.-L. Dyes Depollution of Water Using Porous $TiO_2$-Based Photocatalysts. *Environ. Nanotechnol.* **2020**, *4*, 35–92. [CrossRef]

3. Moridon, S.N.F.; Arifin, K.; Yunus, R.M.; Minggu, L.J.; Kassim, M.B. Photocatalytic Water Splitting Performance of $TiO_2$ Sensitized by Metal Chalcogenides: A Review. *Ceram. Int.* **2022**, *48*, 5892–5907. [CrossRef]
4. Wang, H.; Zhang, L.; Chen, Z.; Hu, J.; Li, S. Semiconductor Heterojunction Photocatalysts: Design, Construction, and Photocatalytic. *Chem. Soc. Rev.* **2014**, *43*, 5234–5244. [CrossRef]
5. Schneider, J.; Matsuoka, M.; Takeuchi, M.; Zhang, J.; Horiuchi, Y.; Anpo, M.; Bahnemann, D.W. Understanding $TiO_2$ photocatalysis: Mechanisms and Materials. *Chem. Rev.* **2014**, *114*, 9919–9986. [CrossRef]
6. Liu, Y.; Wang, M.; Li, D.; Fang, F.; Huang, W. Engineering Self-Doped Surface Defects of Anatase $TiO_2$ Nanosheets for Enhanced Photocatalytic Efficiency. *Appl. Surf. Sci.* **2021**, *540*, 148330. [CrossRef]
7. Baig, U.; Uddin, M.K.; Sajid, M. Surface Modification of $TiO_2$ Nanoparticles Using Conducting Polymer Coating: Spectroscopic, Structural, Morphological Characterization and Interaction with Dye Molecules. *Mater. Today Commun.* **2020**, *25*, 101534. [CrossRef]
8. Gu, S.; Liu, X.; Wang, H.; Liu, Z.; Xing, H.; Yu, L. Preparation and Characterization of $TiO_2$ Photocatalytic Composites Supported by Blast Furnace Slag Fibres for Wastewater Degradation. *Ceram. Int.* **2023**, *49*, 5180–5188. [CrossRef]
9. Lozano, H.; Devis, S.; Aliaga, J.; Alegría, M.; Guzmán, H.; Villarroel, R.; Benavente, E.; González, G. Two-Dimensional Titanium Dioxide—Surfactant Photoactive Supramolecular Networks: Synthesis, Properties, and Applications for the Conversion of Light Energy. *Int. J. Mol. Sci.* **2022**, *23*, 4006. [CrossRef]
10. Benavente, E.; Maldonado, C.; Devis, S.; Diaz, L.; Lozano, H.; Sotomayor-Torres, C.; González, G. A Hybrid Organic-Inorganic Layered $TiO_2$ Based Nanocomposite for Sunlight Photocatalysis. *RSC Adv.* **2016**, *6*, 18538–18541. [CrossRef]
11. Ismail, A.A.; Bahnemann, D.W.; Robben, L.; Yarovyi, V.; Wark, M. Palladium Doped Porous Titania Photocatalysts: Impact of Mesoporous Order and Crystallinity. *Chem. Mater.* **2010**, *22*, 108–116. [CrossRef]
12. Khan, H.; Shah, M.U.H. Modification Strategies of $TiO_2$ Based Photocatalysts for Enhanced Visible Light Activity and Energy Storage Ability: A Review. *J. Environ. Chem. Eng.* **2023**, *11*, 111532. [CrossRef]
13. Le, T.K.; Kang, M.; Kim, S.W. A Review on the Optical Characterization of $V_2O_5$ Micro-Nanostructures. *Ceram. Int.* **2019**, *45*, 15781–15798. [CrossRef]
14. Li, Y.; Chen, S.; Duan, W.; Nan, Y.; Ding, D.; Xiao, G. Research Progress of Vanadium Pentoxide Photocatalytic Materials. *RSC Adv.* **2023**, *13*, 22945–22957. [CrossRef] [PubMed]
15. Sajid, M.M.; Shad, N.A.; Javed, Y.; Khan, S.B.; Zhang, Z.; Amin, N.; Zhai, H. Preparation and Characterization of Vanadium Pentoxide ($V_2O_5$) for Photocatalytic Degradation of Monoazo and Diazo Dyes. *Surf. Interfaces* **2020**, *19*, 100502. [CrossRef]
16. Jayaraj, S.K.; Sadishkumar, V.; Arun, T.; Thangadurai, P. Enhanced Photocatalytic Activity of V2O5 Nanorods for the Photodegradation of Organic Dyes: A Detailed Understanding of the Mechanism and Their Antibacterial Activity. *Mater. Sci. Semicond. Process* **2018**, *85*, 122–133. [CrossRef]
17. Nadolska, M.; Szkoda, M.; Trzciński, K.; Niedziałkowski, P.; Ryl, J.; Mielewczyk-Gryń, A.; Górnicka, K.; Prześniak-Welenc, M. Insight into Potassium Vanadates as Visible-Light-Driven Photocatalysts: Synthesis of V(IV)-Rich Nano/Microstructures for the Photodegradation of Methylene Blue. *Inorg. Chem.* **2022**, *61*, 9433–9444. [CrossRef]
18. Guo, J.; Liang, J.; Yuan, X.; Jiang, L.; Zeng, G.; Yu, H.; Zhang, J. Efficient Visible-Light Driven Photocatalyst, Silver (Meta)Vanadate: Synthesis, Morphology and Modification. *Chem. Eng. J.* **2018**, *352*, 782–802. [CrossRef]
19. Sadeghzadeh-Attar, A. Enhanced Photocatalytic Hydrogen Evolution by Novel Nb-Doped $SnO_2/V_2O_5$ Heteronanostructures under Visible Light with Simultaneous Basic Red 46 Dye Degradation. *J. Asian Ceram. Soc.* **2020**, *8*, 662–676. [CrossRef]
20. Mkhalid, I.A.; Ismail, A.A.; Hussein, M.A.; Al thomali, R.H.M. Visible-Light-Induced V2O5 -TiO2 Photocatalysts with High Photocatalytic Ability for Degradation of Tetracycline. *Opt. Mater.* **2023**, *135*, 113263. [CrossRef]
21. Benavente, E.; González, G.; Cifuentes, N.; Sotomayor-Torres, C.; Aliaga, J. Enhancement Photocatalytic Activity of the Heterojunction of Two-Dimensional Hybrid Semiconductors $ZnO/V_2O_5$. *Catalysts* **2018**, *8*, 374. [CrossRef]
22. Navas, D.; Donoso, J.P.; Magon, C.; Sotomayor-Torres, C.M.; Moreno, M.; Lozano, H.; Benavente, E.; González, G. Ammonium Hexadeca-Oxo-Heptavanadate Microsquares. A New Member in the Family of the $V_7O_{16}$ Mixed-Valence Nanostructures. *New J. Chem.* **2019**, *43*, 17548–17556. [CrossRef]
23. O'Dwyer, C.; Navas, D.; Lavayen, V.; Benavente, E.; Santa Ana, M.A.; González, G.; Newcomb, S.B.; Sotomayor Torres, C.M. Nano-Urchin: The Formation and Structure of High-Density Spherical Clusters of Vanadium Oxide Nanotubes. *Chem. Mater.* **2006**, *18*, 3016–3022. [CrossRef]
24. Benavente, E.; Aliaga, J.; González, G. Chapter 14: Vanadium Oxides in Photocatalysis, Including Bare Oxides and VOx-Based Organic-Inorganic Nanocomposites. In *Vanadium Catalysis*; Sutradhar, M., Pombeiro, A.J.L., da Silva, J.A.L., Eds.; Royal Society of Chemistry: London, UK, 2020; pp. 340–373. [CrossRef]
25. Liu, G.; Greedan, J.E. Magnetic Properties of Fresnoite-Type Vanadium Oxides: $A_2V_3O_8$ (A = K, Rb, NH4). *J. Solid. State Chem.* **1995**, *114*, 499–505. [CrossRef]
26. Lumsden, M.D.; Nagler, S.E.; Sales, B.C.; Tennant, D.A.; McMorrow, D.F.; Lee, S.H.; Park, S. Magnetic Excitation Spectrum of the Square Lattice S = 1/2 Heisenberg Antiferromagnet $K_2V_3O_8$. *Phys. Rev. B* **2006**, *74*, 214424. [CrossRef]
27. Rai, R.C.; Cao, J.; Musfeldt, J.L.; Singh, D.J.; Wei, X.; Jin, R.; Zhou, Z.X.; Sales, B.C.; Mandrus, D. Magnetodielectric Effect in the S=1/2 Quasi-Two-Dimensional Antiferromagnet $K_2V_3O_8$. *Phys. Rev. B* **2006**, *73*, 075112. [CrossRef]
28. Xu, G.; He, H.; Wan, H.; Liu, R.; Zeng, X.; Sun, D.; Huang, X.; Wang, H. Facile Synthesis and Lithium Storage Performance of $(NH_4)_2V_3O_8$ Nanoflakes. *J. Appl. Electrochem.* **2016**, *46*, 879–885. [CrossRef]

29. Pang, H.; Song, Q.; Tian, P.; Cheng, J.; Zou, N.; Ning, G. Non-Hydrothermal Synthesis of $(NH_4)_2V_3O_8$ Hierarchical Flowers and Their Conversion into $V_2O_5$ for Lithium Ion Battery. *Mater. Lett.* **2016**, *171*, 5–9. [CrossRef]
30. Zhang, Y.; Zheng, J.; Wang, Q.; Zhang, S.; Hu, T.; Meng, C. One-Step Hydrothermal Preparation of $(NH_4)_2V_3O_8$/Carbon Composites and Conversion to Porous $V_2O_5$ Nanoparticles as Supercapacitor Electrode with Excellent Pseudocapacitive Capability. *Appl. Surf. Sci.* **2017**, *423*, 728–742. [CrossRef]
31. Chen, X.; Zhang, H.; Liu, J.H.; Gao, Y.; Cao, X.; Zhan, C.; Wang, Y.; Wang, S.; Chou, S.L.; Dou, S.X.; et al. Vanadium-Based Cathodes for Aqueous Zinc-Ion Batteries: Mechanism, Design Strategies and Challenges. *Energy Storage Mater.* **2022**, *50*, 21–46. [CrossRef]
32. Ren, T.Z.; Yuan, Z.Y.; Zou, X. Crystal Growth of Mixed-Valence Ammonium Vanadates. *Cryst. Res. Technol.* **2007**, *42*, 317–320. [CrossRef]
33. Popov, I.S.; Zakharova, G.S.; Liu, Y.; Enyashin, A.N. Relative Stability, Electronic and Structural Properties in the Family of $NH_4V_3O_7$ Polymorphs from First Principles Calculations. *Comput. Theor. Chem.* **2015**, *1070*, 9–13. [CrossRef]
34. Theobald, F.R.; Theobald, J.G.; Vedrine, J.C.; Clad, R.; Renard, J. Crystal Growth, Structure, Electron Paramagnetic Resonance and Magnetic Properties of $(NH_4)_2V_3O_8$. *J. Phys. Chem. Solids* **1984**, *45*, 581–587. [CrossRef]
35. Paraskevopoulou, A.; Pandis, P.; Argirusis, C.; Sourkouni, G. Sonochemical Synthesis of Indium Nitride Nanoparticles and Photocatalytic Composites with Titania. *Ceramics* **2024**, *7*, 478–490. [CrossRef]
36. Bubacz, K.; Kusiak-Nejman, E.; Tryba, B.; Morawski, A.W. Investigation of OH Radicals Formation on the Surface of $TiO_2$/N Photocatalyst at the Presence of Terephthalic Acid Solution. Estimation of Optimal Conditions. *J. Photochem. Photobiol. A Chem.* **2013**, *261*, 7–11. [CrossRef]
37. Livage, J. Hydrothermal Synthesis of Nanostructured Vanadium Oxides. *Materials* **2010**, *3*, 4175–4195. [CrossRef] [PubMed]
38. Baran, E.J. Structural and Spectroscopic Studies Related to Vanadium Chemistry and Biochemistry. *Coord. Chem. Rev.* **2024**, *502*, 215549. [CrossRef]
39. Krumeich, F.; Muhr, H.J.; Niederberger, M.; Bieri, F.; Schnyder, B.; Nesper, R. Morphology and Topochemical Reactions of Novel Vanadium Oxide Nanotubes. *J. Am. Chem. Soc.* **1999**, *121*, 8324–8331. [CrossRef]
40. Pérez-Benítez, A.; Bernès, S. Redetermination of Diammonium Trivanadate, $(NH_4)_2V_3O_8$. *IUCrdata* **2020**, *5*, x200488. [CrossRef]
41. Zakharova, G.S.; Enyashin, A.N.; Podval'naya, N.V.; Zhuravlev, N.A.; Kuznetsov, M.V.; Gorodetsky, R.S.; Liu, Y.; Zhu, Q. Structural, Electronic Properties of Microscale $(NH_4)_2V_3O_8$ Fabricated Using a Novel Preparation Method. *J. Phys. Chem. Solids* **2017**, *101*, 58–64. [CrossRef]
42. Infrared and Raman Characteristic Group Frequencies. *Tables and Charts George Socrates*, 3rd ed.; John Wiley and Sons, Ltd.: Chichester, UK, 2001.
43. Czamara, K.; Majzner, K.; Pacia, M.Z.; Kochan, K.; Kaczor, A.; Baranska, M. Raman Spectroscopy of Lipids: A Review. *J. Raman Spectrosc.* **2015**, *46*, 4–20. [CrossRef]
44. Jokisaari, J.R.; Bayerl, D.; Zhang, K.; Xie, L.; Nie, Y.; Schlom, D.G.; Kioupakis, E.; Graham, G.W.; Pan, X. Polarization-Dependent Raman Spectroscopy of Epitaxial $TiO_2$(B) Thin Films. *Chem. Mater.* **2015**, *27*, 7896–7902. [CrossRef]
45. Alegría, M.; Aliaga, J.; Ballesteros, L.; Sotomayor-Torres, C.; González, G.; Benavente, E. Layered Nanocomposite 2D-$TiO_2$ with $Cu_2O$ Nanoparticles as an Efficient Photocatalyst for 4-Chlorophenol Degradation and Hydrogen Evolution. *Top Catal.* **2020**, *64*, 167–180. [CrossRef]
46. Narayana, M.; Kevan, L. Reinterpretation of the State of Paramagnetic Vanadium Species in Aluminophosphates. *J. Phys. C Solid State Phys.* **1983**, *16*, L863. [CrossRef]
47. Davidson, A.; Che, M. Temperature-Induced Diffusion of Probe Vanadium (IV) Ions into the Matrix of Titanium Dioxide as Investigated by ESR Techniques. *J. Phys. Chem.* **1992**, *96*, 9909–9915. [CrossRef]
48. Jakes, P.; Eichel, R.A. Characterization of Tetravalent Vanadium Functional Centres in Metal Oxides Derived from a Spin-Hamiltonian Analysis. *Mol. Phys.* **2012**, *110*, 277–282. [CrossRef]
49. Ravikumar, R.V.S.S.N.; Rajagopal Reddy, V.; Chandrasekhar, A.V.; Reddy, B.J.; Reddy, Y.P.; Rao, P.S. Tetragonal Site of Transition Metal Ions Doped Sodium Phosphate Glasses. *J. Alloys Compd.* **2002**, *337*, 272–276. [CrossRef]
50. Joy, P.A.; Vasudevan, S. Magnetism and Spin Dynamics in MnPS3 and Pyridine Intercalated MnPS3: An Electron Paramagnetic Resonance Study. *J. Chem. Phys.* **1993**, *99*, 4411–4422. [CrossRef]
51. Murphy, A.B. Band-Gap Determination from Diffuse Reflectance Measurements of Semiconductor Films, and Application to Photoelectrochemical Water-Splitting. *Sol. Energy Mater. Sol. Cells* **2007**, *91*, 1326–1337. [CrossRef]
52. Lee, D.E.; Moru, S.; Reddy, K.P.; Jo, W.K.; Tonda, S. 2D/2D $BiOIO_3$/g-$C_3N_4$ S-Scheme Hybrid Heterojunction with Face-to-Face Interfacial Contact for Effective Photocatalytic $H_2$ Production and Norfloxacin Degradation. *J. Mater. Sci. Technol.* **2023**, *148*, 19–30. [CrossRef]
53. Yong, X.; Schoonen, M.A.A. The Absolute Energy Positions of Conduction and Valence Bands of Selected Semiconducting Minerals. *Am. Mineral.* **2000**, *85*, 543–556. [CrossRef]
54. Hu, Y.; Li, D.; Zheng, Y.; Chen, W.; He, Y.; Shao, Y.; Fu, X.; Xiao, G. BiVO4/TiO2 Nanocrystalline Heterostructure: A Wide Spectrum Responsive Photocatalyst towards the Highly Efficient Decomposition of Gaseous Benzene. *Appl. Catal. B* **2011**, *104*, 30–36. [CrossRef]
55. Gurulakshmi, M.; Selvaraj, M.; Selvamani, A.; Vijayan, P.; Sasi Rekha, N.R.; Shanthi, K. Enhanced Visible-Light Photocatalytic Activity of V2O 5/S-TiO2 Nanocomposites. *Appl. Catal. A Gen.* **2012**, *449*, 31–46. [CrossRef]

56. Wang, Y.; Su, Y.R.; Qiao, L.; Liu, L.X.; Su, Q.; Zhu, C.Q.; Liu, X.Q. Synthesis of One-Dimensional $TiO_2/V_2O_5$ Branched Heterostructures and Their Visible Light Photocatalytic Activity towards Rhodamine B. *Nanotechnology* **2011**, *22*, 225702. [CrossRef] [PubMed]
57. Sun, J.; Li, X.; Zhao, Q.; Ke, J.; Zhang, D. Novel $V_2O_5/BiVO_4/TiO_2$ Nanocomposites with High Visible-Light-Induced Photocatalytic Activity for the Degradation of Toluene. *J. Phys. Chem. C* **2014**, *118*, 10113–10121. [CrossRef]
58. Grätzel, M. Photoelectrochemical Cells. *Nature* **2001**, *414*, 338–344. [CrossRef] [PubMed]
59. Shao, G. Work Function and Electron Affinity of Semiconductors: Doping Effect and Complication Due to Fermi Level Pinning. *Energy Environ. Mater.* **2021**, *4*, 273–276. [CrossRef]
60. Benavente, E.; Navas, D.; Devis, S.; Segovia, M.; Sotomayor-Torres, C.; González, G. Composites of Laminar Nanostructured ZnO and VOx-Nanotubes Hybrid as Visible Light Active Photocatalysts. *Catalysts* **2018**, *8*, 93. [CrossRef]